



Contents lists available at SciVerse ScienceDirect

Nuclear Instruments and Methods in Physics Research A

journal homepage: www.elsevier.com/locate/nima



Effects of geochemical composition on neutron die-away measurements: Implications for Mars Science Laboratory's Dynamic Albedo of Neutrons experiment

C. Hardgrove ^{a,*}, J. Moersch ^b, D. Drake ^b

^a Department of Earth and Planetary Science, University of Tennessee, Knoxville, TN, USA

^b Techsource, Santa Fe, NM, USA

ARTICLE INFO

Article history:

Received 17 March 2011

Received in revised form

24 August 2011

Accepted 25 August 2011

Available online 10 September 2011

Keywords:

Neutron die-away

Mars Science Laboratory (MSL)

Dynamic Albedo of Neutrons (DAN)

Monte Carlo N-particle eXtended code
(MCNPX)

ABSTRACT

The Dynamic Albedo of Neutrons (DAN) experiment, part of the scientific payload of the Mars Science Laboratory (MSL) rover mission, will have the ability to assess both the abundance and the burial depth of subsurface hydrogen as the rover traverses the Martian surface. DAN will employ a method of measuring neutron fluxes called "neutron die-away" that has not been used in previous planetary exploration missions. This method requires the use of a pulsed neutron generator that supplements neutrons produced via spallation in the subsurface by the cosmic ray background. It is well established in neutron remote sensing that low-energy (thermal) neutrons are sensitive not only to hydrogen content, but also to the macroscopic absorption cross-section of near-surface materials. To better understand the results that will be forthcoming from DAN, we model the effects of varying abundances of high absorption cross-section elements that are likely to be found on the Martian surface (Cl, Fe) on neutron die-away measurements made from a rover platform. Previously, the Mars Exploration Rovers (MER) Spirit and Opportunity found that elevated abundances of these two elements are commonly associated with locales that have experienced some form of aqueous activity in the past, even though hydrogen-rich materials are not necessarily still present. By modeling a suite of H and Cl compositions, we demonstrate that (for abundance ranges reasonable for Mars) both the elements will significantly affect DAN thermal neutron count rates. Additionally, we show that the timing of thermal neutron arrivals at the detector can be used together with the thermal neutron count rates to independently determine the abundances of hydrogen and high neutron absorption cross-section elements (the most important being Cl). Epithermal neutron die-away curves may also be used to separate these two components. We model neutron scattering in actual Martian compositions that were determined by the MER Alpha Proton X-Ray Spectrometer (APXS), as examples of local geochemical anomalies that DAN would be sensitive to if they were present at the MSL landing site. These MER targets, named "Eileen Dean," "Jack Russell," and "Kenosha Comets," all have unusually high or low Cl or Fe abundances as a result of geochemical interactions involving water. Using these examples we demonstrate that DAN can be used not only to assess the amount of present-day hydrogen in the near-surface but also to identify locations that may preserve a geochemical record of past aqueous processes.

© 2011 Elsevier B.V. All rights reserved.

1. Introduction

The Mars Science Laboratory (MSL) mission, currently scheduled to launch in late 2011, will carry the Dynamic Albedo of Neutrons (DAN) instrument to the surface of Mars onboard the rover "Curiosity" [1]. DAN will measure the spatial variability in the energy distributions of neutrons emitted from the Martian surface. DAN measurements of neutron energies will be used to provide estimates of, or constraints on, total subsurface hydrogen

content, stratigraphy, and composition in the top ~50 cm of the Martian surface as it traverses. The landing site for MSL will be in the equatorial region of Mars, where orbital neutron measurements made by the Mars Odyssey Neutron Spectrometer (MONS) indicate that near-surface hydrogen content varies between 2 and 10 wt% water-equivalent hydrogen (WEH) [2,3]. Although variations in neutron energies in these latitudes are thought to be primarily due to variations in near-surface hydrogen abundance (e.g., bound in hydrated minerals), variation in the abundance of other elemental constituents (e.g., caused by local changes in rock or soil composition, the degree of alteration, or the presence of salts), would also affect neutron energy distributions through preferential absorption of low-energy neutrons. Because the

* Corresponding author. Tel.: +1 865 748 3837.

E-mail address: craig.hardgrove@stonybrook.edu (C. Hardgrove).

orbital MONS measurements have a large spatial footprint (~ 550 km diameter, FWHM), little is known about the small-scale spatial variability of hydrogen abundance in the equatorial latitudes. In regions where hydrogen abundance varies little, the dominant source of variation in neutron energy distributions will come from variability in other elements, particularly those with high neutron absorption cross-sections. On the lunar surface, the elements Gd and Sm were found to have a pronounced effect on neutron energies [4]. On Mars, Diez et al. [5] have shown that Cl has a significant effect on neutron energy distributions. The Mars Exploration (MER) Rovers have identified an array of rock and regolith types with significant variations in Cl and Fe abundance. Therefore, the purpose of this work will be to characterize the effects of variations in high neutron absorbing elements, particularly Cl and Fe, on the neutron die-away measurements that will be made by DAN.

2. Background

2.1. Neutron die-away

The neutron die-away technique has been used in the oil and gas exploration industry since the early 1960s, and most previous studies of the technique have focused on borehole geometries relevant to this application. DAN is the first spacecraft-based experiment to implement the neutron die-away technique. A detailed overview of the physics of neutron die-away is provided by Adler and Trombka [6]. Neutron die-away measurements are initiated by producing a series of fast neutron (14.1 MeV) pulses with a small accelerator, called a pulsed neutron generator (PNG). The high-energy neutrons from a given pulse penetrate into the surface, where they are scattered and/or absorbed. A portion of the scattered neutrons exit the surface and can be measured by a neutron detection subsystem. These “leaked” neutrons have a new energy distribution that is dependent on the amount of hydrogen in the near surface, the depth of the buried hydrogen, and the macroscopic absorption cross-section of the near-surface material. Hydrogen acts to shift the energy distribution to lower energies (i.e., moderate the energy distribution) because neutrons give up much of their kinetic energy in scattering interactions with the lightweight hydrogen nuclei. If hydrogen is distributed homogeneously in the sub-surface, higher total hydrogen content means fewer high-energy neutrons from the PNG will interact with materials at greater depths. Higher hydrogen content thus shifts the mean arrival time of thermal neutrons to earlier times. If the hydrogen is instead confined to a layer, increasing the burial depth of the hydrogen-rich layer will also shift the neutron energy distribution to lower energies and will shift the average arrival of thermal neutrons at the detectors to later times because the thermalized neutrons will take longer to reach the detector. A high abundance of high absorption cross-section elements will result in an overall decrease of thermal neutrons that can be detected because these elements preferentially absorb thermal neutrons, removing them from the energy distribution in the population of leaked neutrons.

In the neutron die-away method, neutron counts from the detector subsystem are binned by time intervals that are much smaller than the total duration of the neutron die-away. Higher-energy (faster) neutrons arrive at the detectors first, while lower-energy (slower) neutrons arrive at the detectors later. Discrimination of higher- versus lower-energy neutrons is provided through the use of a jacket of cadmium on one of the two detector tubes. Cd has a high absorption coefficient for low-energy neutrons; so this tube will only count higher-energy neutrons. The other (non-Cd wrapped, or “bare”) tube is sensitive to both higher- and

lower-energy neutrons; so differencing the counts between the two tubes provides the counts of lower-energy neutrons. As is the convention in previous studies of planetary neutron remote sensing, in this work we refer to low-energy neutrons (those below the cadmium capture cutoff energy of ~ 0.3 eV) as “thermal.” Energies above 0.3 eV are referred to as “epithermal.”

The overall number of thermal and epithermal neutrons and arrival times of thermal neutrons for a layered subsurface are a function of the hydrogen content of each layer, the layer depths, and the macroscopic absorption cross-section of each layer in the near-subsurface (~ 50 cm) [1,7]. Unfortunately, the changes produced by each of these variables on the thermal neutron die-away curve are non-unique; so it is not possible to independently derive these physical parameters of the subsurface from thermal neutron die-away measurements alone. Rather, candidate models of the subsurface must be used to find combinations of parameters that are consistent with the measurements. The family of subsurface models that are consistent with the measurements can then be further constrained using arguments of geologic plausibility based on other relevant measurements from other instruments. We will show how changes in hydrogen abundances and macroscopic absorption cross-sections that are plausible for Mars can affect both neutron arrival times at the detector and the total thermal and epithermal neutron fluxes.

2.2. Dynamic albedo of neutrons (DAN) instrument

The DAN instrument will utilize the neutron die-away technique as described above. Nominally, the DAN PNG produces 14.1 MeV neutrons at an interval of 100 ms (10 Hz), in pulses with durations of 1 μ s. DAN has one unshielded detector, and one detector coated in a 1-mm-thick layer of Cd, for energy discrimination purposes as described above. Each detector consists of a 6-cm-long by 5-cm-diameter cylinder filled with ^3He pressurized at 3 atm [1]. The detector tubes are proportional counters, in that the charge deposited within the tube is proportional to the sum of the incident neutron energy and the energy of the $^3\text{He}-\text{n}$ reaction [8]. The charge deposited within the tube is then sent through a series of pulse shaping and signal processing circuits housed within the DAN electronics box. The counts are then binned by time and the resulting thermal neutrons are calculated by differencing the counts on the uncoated tube and the counts on the Cd-coated tube. The epithermal neutron counts are simply the counts on the Cd-coated tube.

In all previous implementations of neutron detectors for planetary exploration spacecraft (Mars Odyssey [9,10], Lunar Reconnaissance Orbiter [11], Lunar Prospector [12–14], Messenger [15,16], DAWN [17]), high-energy galactic cosmic rays were relied on to provide neutrons through spallation reactions with nuclei in the planetary surface. These neutrons interact with and subsequently leak from the surface, where they can be detected. Measuring neutrons from a rover platform offers two advantages over orbital measurements. First, because the neutron detectors that have been used on spacecraft missions are not directionally sensitive, the effective footprint of the instrument is proportional to the detector’s height above the ground, such that a rover-based instrument has an effective horizontal footprint of ~ 1 m as opposed to an orbital-based instrument with an effective footprint of (for Mars orbiters) ~ 550 km [18]. Second, the proximity of the ground in a rover-based detector allows for the use of an active neutron source (the PNG), which (as previously discussed) makes discrimination of subsurface layering possible and allows for shorter integration times.

A full instrument description for DAN, as well as modeling results, showing thermal neutron die-away curves for 0–25 wt% water, are provided by Litvak et al. [1]. Additionally, Litvak et al. [19] present modeled results for a sample transect of the DAN

instrument over a hydrogen-rich target, as well as for a buried layer of the (hydrated) smectite clay mineral nontronite. Busch and Aharonson [7] have used model results to derive an empirical equation for determining subsurface water content from thermal neutron die-away curves, taking into account variations in density, the depth to a buried hydrogen-rich layer, and the amount of hydrogen in the upper and lower layers. To the extent that the assumptions of the model (e.g., perfect detection and use of appropriate modeled soil compositions) are met, this equation can be used with DAN measurements to constrain the water content in the top 50 cm of the near surface to within 1 wt%. When the hydrogen content of the near surface is known, either through other instruments or assumption, the analytical solution provided by Busch et al. [7] can also be used to constrain the hydrogen stratigraphy of the top 15 cm of the near surface.

While the work described above will be significant in helping understand future results from DAN, it only takes into account the effects of variations in macroscopic scattering cross-sections for geologic surfaces on the thermal neutron die-away curves. Total macroscopic scattering, which is primarily a function of the abundance of hydrogen, affects the energies of neutrons leaking from the near surface by increasing the number of low-energy (thermal) neutrons and decreasing the number of higher-energy (epithermal) neutrons. Not considered by Litvak et al. [1,10] or Busch et al. [7] was another important effect, that of variations in the total macroscopic absorption cross-section of the near-surface composition. The macroscopic absorption cross-section, which is determined by the neutron absorption cross-sections of the elemental constituents of the near-surface materials weighted by their abundances, can significantly reduce thermal neutron flux through the removal of thermal neutrons from the leaked energy distribution [5,20]. Previous studies on the effects of neutron macroscopic absorption cross-sections have only considered the case of orbital neutron detection with cosmic background as a source, whereas in this study, we explore the effects of macroscopic absorption cross-section on neutron measurements made from the surface, using the neutron die-away method employed by DAN.

DAN is likely to acquire data on traverses across thousands of meters of terrain. Given the wide variety of rock and soil types identified by MER, we anticipate that the MSL rover will encounter not only materials with variable amounts of hydrogen, but also rocks and soils of varying elemental compositions (other than hydrogen), produced by a variety of geologic processes. Evaporitic mineral precipitation, acidic weathering, and aqueous alteration are all examples of processes that produce near-surface enrichments or depletions of elements such as chlorine and iron. In this study, we present simulations of thermal and epithermal neutron die-away for geologically plausible compositions containing variable amounts of chlorine and other neutron absorbing elements. We use these results to determine how the effects of varying macroscopic absorption cross-sections can confound interpretations of hydrogen abundances in the near surface.

2.3. Effects of absorption cross-section on neutron flux

Feldman et al. [4] provided a detailed treatment of the effects of variations in scattering and absorption cross-sections on neutron fluxes for orbital neutron measurements with cosmic ray-induced neutrons. They found that when hydrogen content in the Martian regolith is fixed, changes to the macroscopic absorption cross-section dominate the total number of observed thermal neutrons and their energies. In neutron scattering interactions, the approximate magnitude of the neutron energy loss due to scattering with any element is inversely proportional to the element's atomic mass. A hydrogen nucleus, with the same mass as a neutron, reduces a neutron's energy by $\sim 1/2$ with each scattering event.

This magnitude of this effect is represented by the element's scattering cross-section. The absorption cross-section is a measure of the probability that a neutron will be absorbed while transiting 1 cm of a material, and is a function of the energy of the neutron (lower-energy neutrons being more likely to be absorbed). The macroscopic absorption cross-section is the mean of the absorption cross-sections of the individual elements in the material, weighted by their abundance. Therefore, elements with high absorption cross-sections can significantly influence the macroscopic absorption cross-section of the soil or rock if they are abundant. If high thermal neutron absorption cross-section elements are present in a soil, thermalized neutrons will have a greater probability of being captured, thereby reducing the total number of thermal neutrons measured by the detector. If a correction for this effect is not applied during data analysis, the inferred water-equivalent hydrogen content of the soil will be underestimated.

The effects of high absorption cross-section elements on neutron fluxes from planetary surfaces have been studied for several planetary bodies and are shown to be important in the interpretation of hydrogen abundance in the near surface. For the Moon, the effects of the high absorption cross-section elements Gd and Sm on orbital neutron measurements have shown to be important by Feldman et al. [4]. The effects of Cl were used to reinterpret inferred hydrogen burial depths for the central Elysium Planitia region of Mars by Diez et al. [5]. Thermal neutron counts from MONS have been used to constrain the depth of the hydrogen layer; however, uncertainties in surface composition (and thus, the macroscopic absorption cross-section) leads to an uncertainty of $\pm 10\%$ in the depth to the hydrogen layer [21]. Prettyman et al. [22] found that in several regions, a best fit to the MONS total thermal neutron counts could only be achieved by reducing the modeled soil compositions Cl abundance by 80 wt%. While Diez et al. [21] and Prettyman et al. [22] explored a small subset of compositions for orbital neutron measurements of Mars with neutrons induced by the galactic cosmic background, we sample a larger suite of Cl and H₂O abundances for rover-based neutron die-away measurements with a pulsed neutron generator source, as appropriate for the DAN experiment on MSL.

2.4. Variability of H₂O, Fe, and Cl on Mars

MONS epithermal and fast neutron fluxes have been used to create water-equivalent hydrogen (WEH) maps for the entire surface of Mars [3]. WEH was found to vary between 20% and 100% at latitudes poleward of 50° and between 2% and 10% in the equatorial regions between $\pm 45^\circ$ latitude. For our models we vary water-equivalent hydrogen between 0 and 25 wt%, which represents reasonable upper and lower limits on hydrogen abundances for the equatorial regions of Mars, given that the variability may be greater at the local scale than seen in poor spatial resolution orbital measurements.

Geochemical analyses of the Martian surface have revealed a wide range of Cl abundances in both rocks and soils. Analysis of Viking X-Ray Fluorescence (XRF) data showed that the global abundance of Cl in Martian fines is greater than in terrestrial systems [23]. More recently, Pathfinder APXS data have confirmed that Cl can vary significantly on a more local scale [33]. In the regions explored by MER, Alpha Proton X-Ray Spectrometer (APXS) data confirm that Cl abundances through sol 1503 (from arrival on Mars in January, 2004, to March, 2008) vary between 0.2 and 2.6 wt% [25]. While results from both Spirit and Opportunity APXS measurements have shown variability in Cl abundance of surface materials, Spirit's front right wheel trenching has provided a unique observation of sub-surface materials that could also be detected by DAN. This trenching uncovered, in particular, a unique class of high-Cl soils near the feature known as Home

Plate (exemplified by the target named “Eileen Dean”), which was found to contain 1.8 wt% Cl. In addition to relatively high Cl content, Eileen Dean class soils are high in magnetite and Mg (similar to Everett class rocks) and are also enriched in Ni, Zn, and Br, which indicates possible alteration by hydrothermal water or vapors. A possible cause of the elevated Cl abundances in the vicinity of Home Plate was revealed through a detailed study by the Spirit rover over 2 years. Several features were identified, which indicate that the area was a source of volcanism as well as hydrothermal activity [26]. Evidence for extensive low-temperature alteration on the western side of Home Plate was also identified as a possible source for high-Cl deposits [27]. Throughout Gusev crater, several rock classes were found to be enriched in Cl with respect to the Adirondack class basalts, which were found to contain 0.3 wt% Cl. These rocks include the Watchtower class (1.2 wt% Cl), Barnhill class (1.6 wt% Cl), Everett class, and Good Question class (both ~1.4 wt% Cl) [25]. These observations from MER have shown that Cl is variable in Martian surface materials and can be concentrated in localities that have experienced near-surface aqueous alteration.

APXS data have shown that Fe abundances through sol 1503 (from arrival on Mars in January, 2004, to March, 2008) vary between 0.7 and 43 wt% [28]. Regionally, changes in the relative differentiation of parent magmas affect the Fe abundances in basaltic surface rocks on Mars [29]. Although the neutron absorption cross-section of Fe is not as high as Cl, a large enough variation in the abundance of Fe on a local scale could also have a significant effect on the overall neutron flux. Pervasive hematite concretions in Meridiani Planum are suggested to have precipitated from rocks that were exposed to groundwater and subsequently deposited as a lag surface [30]. It may also be possible to distinguish buried hematite-rich (“blueberry”) layers with a

neutron die-away technique, if these materials are enriched in the near surface. Compositions of several Fe- and Cl-rich targets that were identified by Spirit and Opportunity are listed in Table 1.

MER APXS-derived abundances for the highest absorption cross-section elements (Cl, Mn, Ti, and Fe) excluding the Fe-rich meteorite, Heat Shield Rock, are presented in Table 2, along with the average standard deviation for those elements across all APXS measurements. Averages were derived from all APXS measurements of Martian composition, i.e., excluding targets thought to be meteorites that originated elsewhere in the solar system. Of the elements listed in Table 2, Cl and Fe are the best candidates to have significant effects on neutron die-away curves acquired on the Martian surface. Even though elements such as Si and O are more abundant, they both have relatively lower absorption cross-sections and variations in their abundance result in small or negligible effects on the energy distribution of leaked neutrons. Other elements with relatively high absorption cross-sections, such as Mn, Br, and Ti, may also play a role in capturing thermal neutrons; however, they are present in such low abundances and

Table 2

MER Spirit and Opportunity mean APXS abundances (through sol 1503) of the highest absorption cross section elements likely to be encountered on the Martian surface.

Element	Avg. wt%	Standard deviation	Absorption cross-section
Cl	0.89496	0.38780	33.50
Mn	0.23052	0.05787	13.30
Br	0.01378	0.01734	6.90
Ti	0.54807	0.19666	6.09
Fe	12.18295	3.87635	2.56

Table 1

Scattering and absorption cross sections of various elements of geologic interest on Mars. Also shown are weight fractions for all elements used in a bulk Mars soil composition, the Mars Exploration Rover APXS elemental data used for anomalous absorption cross-section compositions, and the range of variation of Cl used in our systematic study.

Elements	Scattering cross-section ^{a,b}	Absorption cross-section ^{a,b}	Gusev basaltic soil mass fraction ^c	Cl-rich Home Plate, “Eileen Dean” ^d	Hematite-rich, “DogPark – Jack Russell” ^e	High-silica, “Kenosha Comets” ^f	Iron meteorite, “Heat Shield Rock” ^g	Variations in Composition
O	4.2320	0.0002	0.4566	0.4321	0.3979	0.5353	–	–
Si	2.1670	0.1710	0.2165	0.2314	0.1767	0.4230	–	–
Al	1.5030	0.2310	0.0535	0.0323	0.0381	0.0005	–	–
Ca	2.8300	0.4300	0.0453	0.0271	0.0368	0.0051	–	–
Fe	11.6200	2.5600	0.1248	0.1251	0.2596	0.0109	0.94	–
Mg	3.7100	0.0630	0.0519	0.0953	0.0386	0.0139	–	–
Na	3.2800	0.5300	0.0223	0.0104	0.0119	0.0024	–	–
Ti	4.3500	6.0900	0.0052	0.0030	0.0042	0.0073	–	–
Mn	2.1500	13.3000	–	0.0019	0.0022	0.0002	–	–
K	1.9600	2.1000	–	0.0035	0.0031	–	–	–
P	3.3120	0.1720	–	0.0029	0.0033	–	–	–
S	1.0260	0.5300	–	0.0124	0.0192	–	–	–
Cr	3.4900	3.0500	–	0.0036	0.0025	–	–	–
Ni	18.5000	4.4900	–	0.0007	0.0011	–	0.07	–
Zn	4.1310	1.1100	–	0.0011	0.0003	–	–	–
Br	5.9000	6.9000	–	0.0001	0.0000	–	–	–
H	82.0200	0.3326	–	–	–	–	–	0–25 wt% as H ₂ O [in 1 wt% increments]
Cl	16.8000	33.5000	0.0072	0.0170	0.0046	0.0014	–	0–5 wt.% [in 0.5 wt% increments]
Cd ^h	6.5000	2520.0000	–	–	–	–	–	–

^a Units in barns.

^b http://www.ncnr.nist.gov/resources/n-lengths/Neutron_News, vol. 3, no. 3, 1992, pp. 29–37.

^c [35].

^d [25].

^e [24].

^f [34].

^g [28].

^h Cadmium is a detector material that coats one ³He tube to filter out neutrons with energies lower (thermalized) than 0.3 eV.

have so little variation in abundance in both Spirit and Opportunity APXS data that their effects on controlling variations in neutron leakage spectra are not expected to be as significant as Cl or Fe. In Section 4, we present results for thermal neutron fluxes where the most abundant elements in Table 2 (Cl, Fe, and Ti) are varied by one APXS-derived standard deviation of each element's abundance. The most variable of these elements is Fe; however, the absorption cross-section of Fe is ~1/13th that of Cl. In addition, APXS-derived Fe abundances vary by ~25% relative to the average Fe abundance while Cl abundances vary by ~33% relative to the average Cl abundance. Due to these factors, we expect the influence of Cl on neutron die-away to be greater than Fe and perform a systematic study to determine the effects of Cl in Section 4.4. We model the effects of Fe using several site-specific examples from MER Spirit and Opportunity in Section 4.5.

Based on the elemental compositional variability presented above and the measured neutron absorption cross-sections presented in Table 1, we hypothesize that the dominant source of variability in surface-measured neutron leakage spectra associated with the macroscopic absorption cross-sections for plausible Martian geochemical compositions is Cl, followed by Fe. We further hypothesize that a neutron detector capable of making die-away measurements (like DAN) will be sensitive to interesting and unusual materials other than hydrogen that are at or below the surface. For example, hydrothermally altered soils, buried high-silica deposits, or hematite concretions, all of which have significantly anomalous macroscopic neutron absorption cross-sections, should be relatively simple to detect by virtue of the effect they have on thermal and epithermal neutron fluxes.

3. Methods

3.1. Monte Carlo modeling

Because there is no analytical model to describe the probabilistic interactions of neutron transport in a variety of geometries, compositions, and energies, we utilize the Monte Carlo N-Particle eXtended (MCNPX) code to model neutron behavior in a suite of subsurface compositions and geometries. MCNPX simulates the transport and interactions of individual neutrons in a user-defined geometry using scattering and absorption coefficients from particle data libraries [31,32]. To determine the effects of soil compositions enriched in high absorption cross-section elements on neutron die-away, MCNPX is used to model the thermal neutron flux for soil compositions that are anomalously rich or poor in these elements in a simple Mars soil composition (described below). A 14.1 MeV fast neutron source at the height of the PNG mounted on the MSL rover (80 cm) is included in the model. All neutron fluxes are reported at the detector position, 80 cm above the ground and 1 cm horizontal from the source, to simulate the DAN detector geometry. In any given simulation, MCNPX models the history of individual neutrons (total number is specified by the user) and data libraries are used as look-up tables for determination of the appropriate scattering and absorption cross-sections for every neutron interaction. There are several data libraries available for neutron cross-section data, and we use the most recently acquired MCNPX cross-section library for each element within the modeled soil composition. The most recent library varies from element to element; thus, several were chosen. These libraries are .50c, .55c, .60c, and .66c of Pelowitz et al. [32]. When discrete cross-section data are not available for the neutron energies involved, MCNPX uses models to derive a best fit. Errors associated with cross-section libraries or model assumptions are propagated throughout the MCNPX

simulation and folded into the reported relative error when the simulation is complete.

Because no DAN instrument response model has been published as of yet, our results for neutron die-away curves and total flux of neutrons arriving at the detector are provided in normalized units of neutrons/cm²/s/source-particle. This value is the total number of neutrons that are incident on 1 cm² at the DAN detector orientation and position per source-particle. For DAN, there are ~10⁷ neutrons emitted per PNG pulse; however, the total number of neutrons detected will be dependent on the pulse rate (in Hz) of the PNG, the integration time, and the efficiency of the detectors and electronics. In Section 5, we discuss the determination of uncertainties in counting rates based on the Poisson statistics to show that the effects we describe should be detectable for typical DAN observations. Another potentially complicating factor is the energy spectrum of neutrons emitted by Mars Science Laboratory's Radioisotope Thermoelectric Generator (RTG). We note, however, that Busch et al. [7] cite an expected uncertainty of less than 10 neutrons/pulse and less than 0.1 neutrons/pulse/time bin for the RTG based on its plutonium content [7]. We, therefore, do not model the effects on neutron fluxes due to the RTG.

To interpret thermal neutron die-away curves quantitatively, we examine both the total neutron flux and the timing component of each die-away curve. To quantify this timing, we define a parameter we call the flux weighted time average (FWTA) as the average arrival time for all thermal neutrons, weighted by the flux at each small time interval of the die-away period:

$$\text{FWTA} = \frac{\sum_{n_i=100\mu s} t_i f_i}{\sum_{n_i=100\mu s} f_i}$$

where t_i represents the time associated with the i th time bin after the pulse, and f_i represents the number of thermal neutrons counted in i th time bin. The FWTA is calculated for thermal neutrons arriving at the detectors after 100 μ s, as it takes a thermal neutron (< 0.3 eV) approximately 100 μ s to travel from the surface to the detectors (80 cm). We discuss the relative changes in thermal and epithermal neutron energy distributions for die-away curves and relative changes to the FWTA for a suite of hydrogen, Cl and Fe abundances that have been chosen based on actual compositions measured on the Martian surface.

For the majority of our model simulations, we have used the Newton cluster computing system, which is housed at the University of Tennessee, Knoxville. The cluster consists of over 250 64-bit computer nodes with a total of over 2400 processor cores and 5 TB of RAM. The high computing capacity of this system allows us to simulate a large number of particles for each run in a relatively short period of time. For example, a standard MCNPX simulation from this work models the transport of 2×10^9 neutrons. Using Newton, with an allocation of only 450 processors, this calculation can be completed in approximately 20 min of “wall clock time,” with low relative errors (< 10%, see Section 5.4, below).

3.2. Compositions

The soil compositions we have modeled fall into two broad suites. The first suite consists of a “typical” Martian basaltic soil that is fixed in composition except for Cl and H₂O contents that systematically vary over a plausible range of abundances. The second suite consists of several “real world” compositional inventories that were previously determined at specific locations on the Martian surface. Compositions from the MER APXS experiment were used to (1) provide elemental abundances for a “typical” Martian soil composition, (2) provide upper and lower

limits on the abundances of Cl used in our systematically varying suite of compositions, and (3) provide complete elemental inventories for specific examples of well-characterized locations on Mars shown to have anomalous abundances of high absorption cross-section elements [17,24,25]. The specific locations from MER were chosen based on their abundance of high absorption cross-section elements (Cl and Fe) and their importance for understanding the aqueous geochemical history of the Martian surface. We recognize that whatever anomalous compositions are encountered by MSL may not be the same as those found by Spirit and Opportunity, but the MER compositions do serve as examples of the variety of geochemically interesting compositions that are possible at a local scale on Mars. Table 1 shows the Mars Exploration Rover APXS data used to set high and low limits on Cl abundances, as well as the bulk “typical” Martian soil composition estimate used in all simulations. Unless otherwise noted, the bulk soil composition in all simulations is the average of all basaltic soil compositions derived from APXS measurements in Gusev crater, as presented in Ref. [35].

Our systematically varying suite of compositions is made up of the bulk Martian soil composition described in Table 1 with a Cl abundance varying from 0 to 5 wt%. We also systematically vary H₂O content from 0 to 25 wt% (based on MONS results [3]). Table 2 shows elemental abundances and variability for high absorption cross-section elements, as derived from MER Spirit and Opportunity APXS soil and rock measurements through the 4th year of both missions. Although 5 wt% Cl is well above reported values by APXS, we have chosen to model these higher abundances for two reasons. First, we expect that a salt-rich deposit, composed of a cation bound to a Cl atom (~50 wt% Cl depending on the cation), should include more than 5 wt% Cl and would be an important location to study for understanding the history of near-surface water on Mars. Such chloride-rich deposits have been postulated by Osterloo et al. [36] as the explanation for spectrally anomalous features observed on the Martian surface in the thermal infrared. Second, as we will demonstrate in Section 6, the effects of Cl in abundances much less than 5 wt% are significant enough to influence thermal neutron die-away curves.

For specific soil compositions, we use APXS geochemical data for well-studied locations on Mars that are thought to have experienced near-surface aqueous activity in the past. As described in Section 4, these compositions are (1) Eileen Dean, a Cl-rich soil described by Ming et al. [25]. We model the subsurface as a continuous (extending infinitely downward) layer of Eileen Dean material under a 4-cm-deep layer of bulk Martian soil and also as a discrete layer, 4 cm thick and 4 cm deep, sandwiched above and below by bulk Martian soil; (2) Jack Russell, a surface consisting principally of hematite-rich “blueberries” found in Eagle Crater [33]. Although such materials would be obvious from camera images if found at the surface (as they were found by Opportunity), it would also be useful to be able to detect buried hematite concretions. To test this possibility, we therefore model the case where these materials have been buried under bulk Martian soil. As with the Eileen Dean models, the buried Jack Russell material is modeled as a continuous layer under 4 cm of bulk soil, and also as a discrete layer 4 cm deep and 4 cm thick; (3) Kenosha Comets, a Si-rich soil found in the Eastern Valley of Gusev Crater [25]. Kenosha Comets is a soil devoid of high scattering and high absorption cross-section elements, such that relatively little neutron moderation can occur. We use the same burial geometries for Kenosha Comets materials as we use for Eileen Dean and Jack Russell materials. The burial depth chosen (4 cm) for all of these model geometries is meant to be typical of depths that could be exposed by trenching with a rover wheel and is not necessarily the exact depth at which these materials were found by the MER rovers [37]. We also model (4) Heat Shield

Rock, which is an iron meteorite discovered by the Opportunity rover [28]. All four specific soil compositions are presented in Table 1 along with the composition of the bulk soil.

3.3. Error

Neutron fluxes calculated in MCNPX for each time step in the neutron die-away process have an associated relative error. This error is a statistical error that describes the convergence of the simulation to the flux value reported. Included within MCNPX are ten statistical tests of the convergence of this reported value, which are run at the end of each simulation. A full description of the statistical tests and reliable values of relative error appears in Ref. [32]. Relative errors of less than 10% are generally reliable, and in this study we only report results for neutron fluxes where the mean relative error is less than 10%. For each of the following sub-sections of Section 6, we report the mean relative error for each set of simulations as well as the resulting uncertainty in neutron flux. It is important to note that this error is purely statistical and does not take into account uncertainties inherent to the measurement of actual neutrons by the DAN detectors and electronics. In this work we demonstrate the expected relative changes in neutron flux for a variety of geologic scenarios. However, we do not provide specific changes in neutron counting rates for the DAN instrument because an instrument response function has not been published. In Section 5, we discuss the uncertainty in count rates for a specific DAN operational mode, based on the Poisson statistics. This analysis is sufficient to determine that the trends reported in Section 5 are detectable, assuming that the uncertainties introduced by the DAN instrument response function, noise, and signal processing electronics are not substantial.

4. Results

4.1. Cosmic background contribution

We first model the thermal and epithermal neutron flux from Galactic Cosmic Rays (GCRs) for DAN observations without including PNG-sourced neutrons to determine whether GCRs-sourced neutrons are a significant component of the flux measured by DAN when the PNG is used. Neutrons produced by GCRs interacting with the surface and atmosphere of Mars result in a steady flux of neutrons whose electronic signals are indistinguishable from those signals produced by the PNG neutrons. We used MCNPX to model the neutron leakage neutron flux. For these calculations we took a small patch of a Martian surface and bombarded it with the usual GCR proton spectrum [38]. To ensure that edge effects of this geometry were not significant, we verified that the leakage flux at different distances from the detector position were essentially the same. The Martian model composition was a generic Martian dirt with 3% water and a 12 g/cm² atmosphere. Both upward and downward fluxes were calculated at the height of the neutron detectors. Because the GCR flux varies in time one must normalize the results. For comparison between PNG and GCR fluxes we take the GCR flux to be 2/cm². The leaked neutron flux in neutrons/cm²/s/source-particle from 1×10^{-9} to 14 MeV is shown in Fig. 1 for both neutrons produced by the PNG and those from GCRs. Uncertainties in flux reported by MCNPX for both PNG and GCR are smaller than the size of the data point symbols in Fig. 1, and so error bars are not shown.

To approximate an example operational mode for DAN, we model the PNG at a pulse frequency of ~10 Hz and a total detector integration time of 30 min. Neutrons from the PNG die away within 0.002 s; so their effective accumulation time is

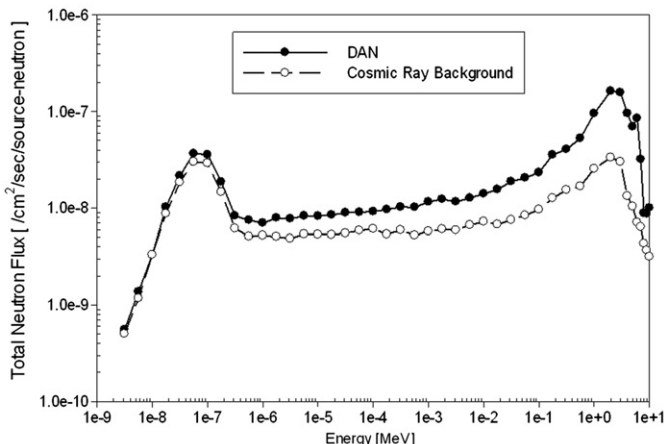


Fig. 1. Neutron flux at the DAN neutron detectors due to the GCR and PNG produced neutrons.

0.6 min. Using timing gates to separate the PNG and GCR data, one can calculate a fluence/cm² of approximately 1.4 thermal neutrons and 2.4 epithermal neutrons from each PNG pulse arrive at the detector, while for GCRs, the fluence of neutrons is 6.7 n/cm² in the 0.1 s between PNG pulses. One can correct the counts in the PNG interval by subtracting 1/49 of the pulses in the GCR interval, which for this exercise is about 3% of those counts. The neutron background due to GCR is, therefore, much smaller than neutrons originating from the PNG. Although the GCR generated neutrons could be analyzed to assess compositions and depths below the PNG sensitivity (~50 cm), we have elected to model only the PNG source and do not include neutrons produced by the GCR. A complete analysis of using GCRs to constrain hydrogen content and burial depth for surface-based neutron measurements is presented in Ref. [39].

4.2. Neutron timing and energy

Next we present an example result for a generic Mars soil composition (Table 1) with 1 wt% H₂O to illustrate the timing of detected neutrons at various energies (thermal, epithermal, and fast). Fig. 2 shows the arrival times for neutrons from 0 to 14 MeV, separated into thermal, epithermal, and fast energy ranges, from the start of the pulse at 0 μs to 1 ms. Note that no thermal neutrons are detected in the first ~100 μs after the PNG pulse, but that all the neutrons coming immediately after this time are thermal neutrons. Qualitatively, the distribution of the three energy ranges over time can be understood in terms of the travel times for neutrons within each energy range. Using the approximation that neutron velocity is proportional to the square root of its energy, we note that high-energy neutrons from the pulse travel at extremely high speeds (> 5000 cm/μs), entering the soil and interacting with the nuclei of the near-surface materials. The amount of time these neutrons spend within the near surface is dependent on the number of interactions they have and how much energy is lost with each interaction. If these high-energy neutrons interact with hydrogen, their energy distribution is shifted to lower energies, thus reducing the speed of these neutrons, increasing the amount of time spent in the near surface, and therefore, the amount of time it will take to scatter out of the surface and reach the detectors. Thermal neutrons (< 0.3 eV) travel approximately 80 cm in 100 μs, consistent with the first arrival time (shown in Fig. 2) of thermal neutrons at a detector mounted 80 cm above the ground, as modeled in MCNPX. Neutrons arriving at earlier times are of higher energy and have interacted with materials closer to the surface. This illustrates

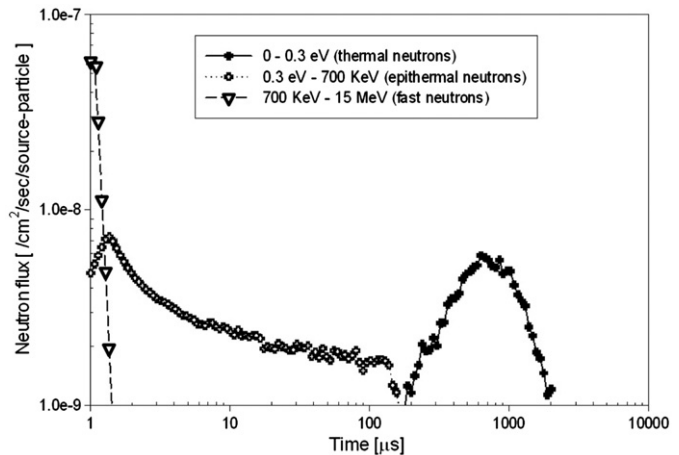


Fig. 2. Example of neutron flux at the ³He neutron detector versus time of arrival ("die-away" curve) for three different neutron energy ranges. For comparison, simulations of GCR induced thermal, epithermal and fast neutron fluxes result in significantly lower values over this duration (0.1 s) and can be represented by lines of constant flux at 1.21×10^{-13} , 1.01×10^{-13} , and 2.25×10^{-13} neutrons/cm²/μs/source-particle, respectively.

how (1) thermal neutrons that arrive at the detector after ~100 μs are sensitive to the scattering and absorption properties of nuclei at depth and (2) analysis of the thermal neutron energy portion of Fig. 2 can be used to interpret geochemical information of the near surface. The mean relative errors in thermal, epithermal, and fast neutron fluxes are 2.40%, 6.91%, and 4.86%, respectively. The resulting mean uncertainties in neutron fluxes for all energy ranges are smaller than the data point symbols in Fig. 2. Therefore, in Fig. 2 and all subsequent figures the error values are not shown but are provided in the appropriate section of the text.

Fig. 3a shows a suite of thermal neutron (only) die-away curves for soils with variable H₂O contents, from 0 to 25 wt%, with the remainder of the soil composition proportioned as shown for bulk soil in Table 1. As hydrogen content of the near surface increases, the total number of thermal neutrons increases and more high-energy source neutrons are moderated to lower energies. This relationship is well understood and constitutes the basis for using thermal neutron measurements to determine subsurface hydrogen content [40]. In addition, the FWTA shifts to earlier times with increasing hydrogen content. Hydrogen is added to the modeled soil homogeneously; therefore, as hydrogen content is increased, neutrons have a greater chance of interaction with hydrogen immediately entering the surface. This results in a shifting of thermal neutron arrival times to earlier times. Fig. 3b shows how the FWTA decreases with increasing H₂O content. As expected from Litvak et al. [1] and Busch et al. [7] the total thermal neutron flux decreases with decreasing H₂O content (~89% from 25 to 0 wt% H₂O) and the FWTA decreases by 14%. Fig. 3a and b shows that as H₂O content increases, the FWTA decreases nearly linearly, while the peak in thermal neutron die-away flux shifts to earlier times as H₂O content increases from 0 to 1 wt% and then to later times as H₂O content increases beyond 1 wt%. This indicates that the FWTA is a more appropriate quantity to use in interpreting trends between various neutron die-away curves than the peak in thermal neutron die-away.

4.3. Effects of Cl, Fe, Ti, Br, and Mn on thermal neutron die-away

To determine which high absorption cross-section elements are most likely to be important in contributing to variability in DAN results from Mars, we have used the MER APXS compositions in Table 1 in a series of sensitivity tests with MCNPX. We use the

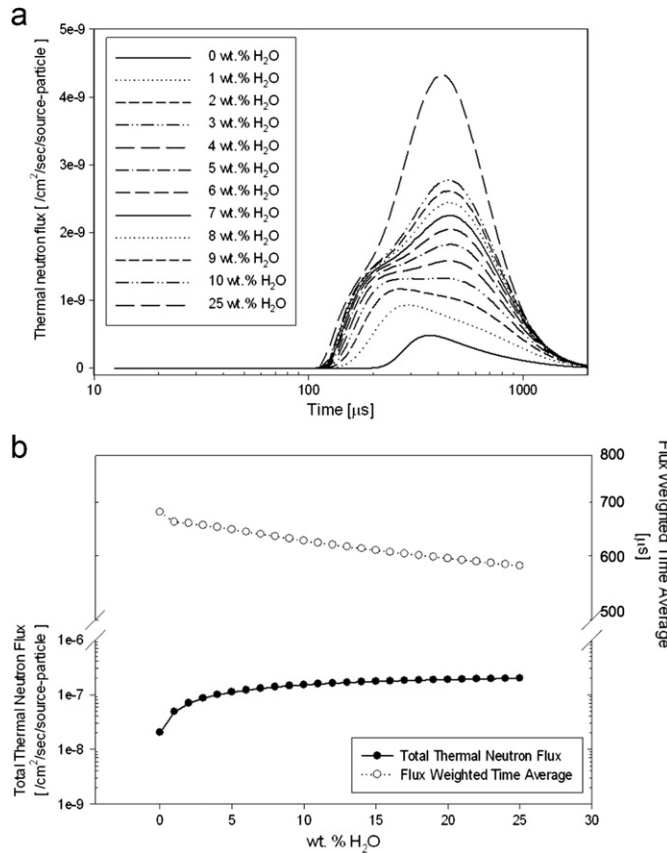


Fig. 3. (a) Arrival times at the detector for thermal neutrons (defined as energies less than 0.3 eV) for selected soil H₂O contents ranging from 0 to 25 wt% and (b) total thermal neutron flux and the flux weighted time average (FWTA) vs. H₂O content with no Cl.

average abundance and standard deviation for each of these elements in the MER measurements, such that our determination of the relative importance of each element is dependent not only on its absorption cross-section, but also on its likely variability during a potential MSL traverse. This approach is based on the reasonable assumption (in the absence of any better information) that the geochemical abundance variations encountered by the MER rovers are analogous to those that will be found at the MSL landing site. For each high absorption cross-section element, Cl, Fe, Ti, Br, and Fe, we perform two MCNPX simulations: one with the average abundance for the element being tested and another in which we increase the average abundance by one standard deviation. In these simulations, we keep a fixed “host” composition of bulk Mars soil (the average composition across all Gusev basaltic soils, shown in Table 1); however, if the element being tested is already in the bulk soil composition, we replace that abundance with the average abundance of that element across all APXS measurements, and then normalize the result. When the element being tested is not present in the bulk soil composition, we add its average abundance to the soil, and then normalize the result. A similar set of simulations is performed in which the abundance of the element being tested is set to the average of that element's abundance across all MER APXS measurements plus one standard deviation of abundance for that element. We compare the modeled neutron flux for the average element abundance to the modeled neutron flux for the (average+one standard deviation) element abundance to determine how important that element is likely to be in contributing variations in the DAN dataset. We find that, in order of decreasing importance, the variability in Cl ($\sigma=0.388$ wt%) changes the total thermal neutron

flux by $\sim 16\%$, the variability in Fe ($\sigma=3.876$ wt%) changes the total thermal neutron flux by $\sim 8.3\%$, the variability in Ti ($\sigma=0.197$ wt%) changes the total thermal neutron flux by 1% , and the variabilities in Mn ($\sigma=0.058$ wt%) and Br ($\sigma=0.017$ wt%) both change the total thermal neutron flux by less than 1% . Based on these analyses and the relative average abundances of these elements (Table 2), we find that Cl and Fe are the most likely candidates among the high neutron absorption cross-section elements to strongly influence variability in DAN measurements.

4.4. Chlorine

We have shown how the total thermal flux increases (Fig. 3a) and the FWTA decreases (Fig. 3b) with increasing H₂O content from 0.5 to 25 wt% and no Cl. To explore the effects of introducing high absorption cross-section elements into the soil, we add 0.5 wt% Cl into the soil as an initial test. The thermal neutron die-away curves for 0 and 0.5 wt% Cl with 0 and 3 wt% H₂O (Fig. 4a) demonstrate the significant effects of Cl on both the total thermal neutron flux as well as the time distribution of thermal neutron arrival times at the detector. The presence of Cl increases the macroscopic absorption cross-section of the soil. The increased absorption of thermal neutrons decreases the total thermal neutron flux. In addition, as the abundance of high absorption cross-section elements increases, neutrons that are thermalized at depth in the sub-surface have an increased probability of interacting with, and subsequently being absorbed by, a high absorption cross-section element. The result is that neutrons from shallower depths have a greater probability of being detected if the soil is enriched in high absorption

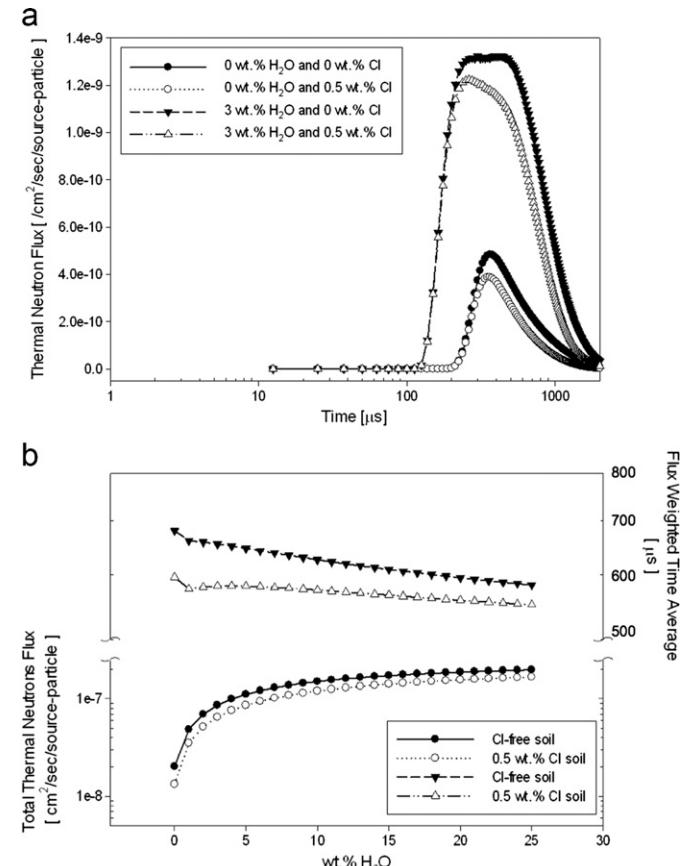


Fig. 4. (a) Arrival times at the detector for neutrons less than 0.3 eV for selected low H₂O and Cl concentrations and (b) the average time of arrival (FWTA) for low-energy neutrons for 0 and 0.5 wt% Cl as a function of H₂O concentration.

cross-section elements, thus shifting the FWTA towards earlier times. Fig. 4b shows the effects of adding 0.5 wt% Cl on the total thermal neutron flux and the FWTA for H₂O contents ranging from 0 to 25 wt%. For low H₂O content (0–5 wt%), adding a small amount of Cl (0.5 wt%) shifts the FWTA to earlier times by approximately 10–12% and reduces the total thermal neutron flux by approximately 28–43%. We find that FWTA values and total neutron flux values are both inversely correlated with Cl content, whereas total neutron flux is directly correlated with H₂O but inversely correlated with Cl. Table 3 shows how the presence of Cl changes the total thermal neutron flux and FWTA for 0, 1, 3, and 5 wt% H₂O and 0, 0.5, and 1 wt% Cl.

The full suites of neutron die-away results for H₂O content varying from 0 to 25 wt% and Cl content varying from 0 to 5 wt% are presented in Figs. 5 and 6. The data are plotted in 3 dimensions (Fig. 5a and b), defining a surface that constrains the thermal neutron fluxes or values of FWTA that are possible for a given H₂O and Cl content mixed into bulk Martian soil. These data are also presented on contour plots, which are shown in Fig. 6a and b.

The results presented in Fig. 5 and 6 and Table 3 demonstrate that interpretations of the hydrogen content evidenced in DAN thermal neutron fluxes may be flawed if Cl content is not known

and correctly taken into account. A surface with 5 wt% H₂O and no Cl would give the same total thermal neutron flux as a surface with 10 wt% H₂O and 0.5 wt% Cl. Similarly, the total thermal flux for 10 wt% H₂O and no Cl is also consistent with almost 18 wt% H₂O and 0.5 wt% Cl. If only the total thermal neutron flux is used in analyses, the presence of small amounts (~ 0.5 wt%) of Cl effectively masks significant amounts of H₂O. Epithermal neutrons and/or the thermal neutron FWTA must be used to separate the effects of high absorption cross-section elements and H₂O.

For the purposes of MSL operations and DAN data analysis, Fig. 6a and b suggests a strategy for using neutron measurements to place constraints on Cl and H₂O content. The total thermal neutron flux from the die-away curve determines a possible suite of paired Cl and H₂O contents, represented as a single contour in Fig. 6a. The correct pair of H₂O and Cl contents from this suite of possible values is found by plotting the appropriate curve from Fig. 6a on the FWTA contour plot in Fig. 6b and observing where the curve of possible paired content values intersects the contour corresponding to the measured FWTA value. The error associated with the unique determination of H₂O and Cl using this method is dependent, in part, on the angle at which the curve extracted from the total neutron flux contour intersects the appropriate

Table 3
Changes in total thermal flux and FWTA for low values of H₂O with increasing Cl.

H ₂ O (wt%)	Cl (wt%)	Total thermal flux ^a	FWTA ^b	% Decrease in thermal flux	% Shift in FWTA	Change in FWTA ^b
0	0	3.00224E−08	680.39	–	–	–
0	0.5	1.71098E−08	596.64	43.01	12.31	83.75
0	1	1.14047E−08	542.99	33.34	8.99	53.65
1	0	6.69765E−08	661.02	–	–	–
1	0.5	4.26062E−08	577.5	36.39	12.64	83.52
1	1	3.13507E−08	523.89	26.42	9.28	53.61
3	0	1.08842E−07	655.19	–	–	–
3	0.5	7.62809E−08	581.77	29.92	11.21	73.42
3	1	5.8596E−08	533.77	23.18	8.25	48.00
5	0	1.37641E−07	647.117	–	–	–
5	0.5	9.92968E−08	581.63	27.86	10.12	65.49
5	1	7.78443E−08	538.62	21.60	7.39	43.01

^a Neutrons/s/cm²/source-particle.

^b μ s.

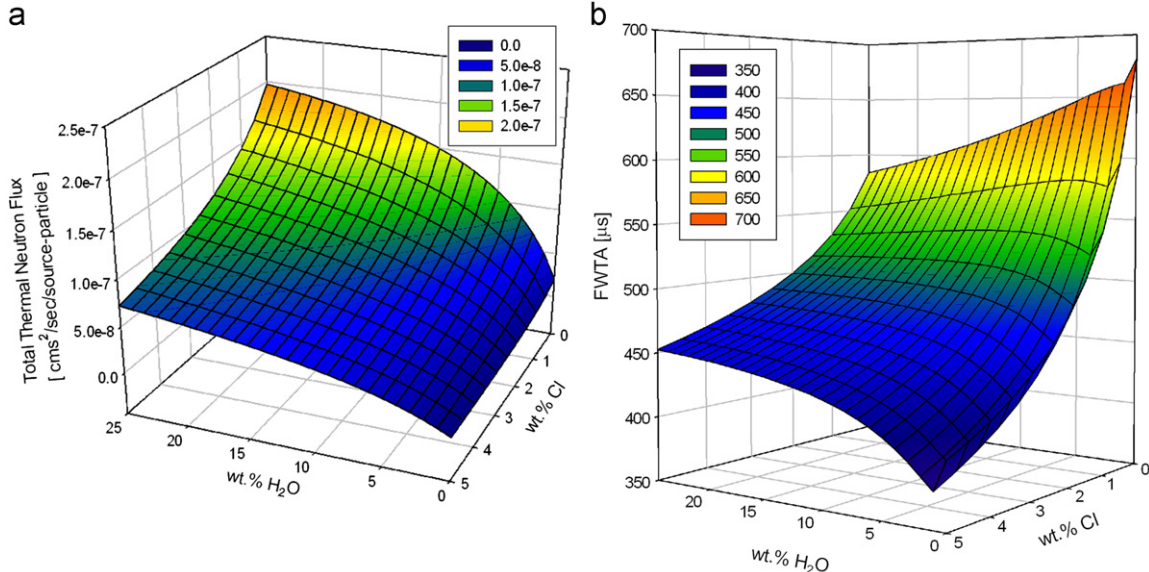


Fig. 5. (a) Surface plot showing the thermal neutron flux as a function of H₂O and Cl concentration and (b) surface plot showing the flux weighted time average (FWTA) as a function of H₂O and Cl.

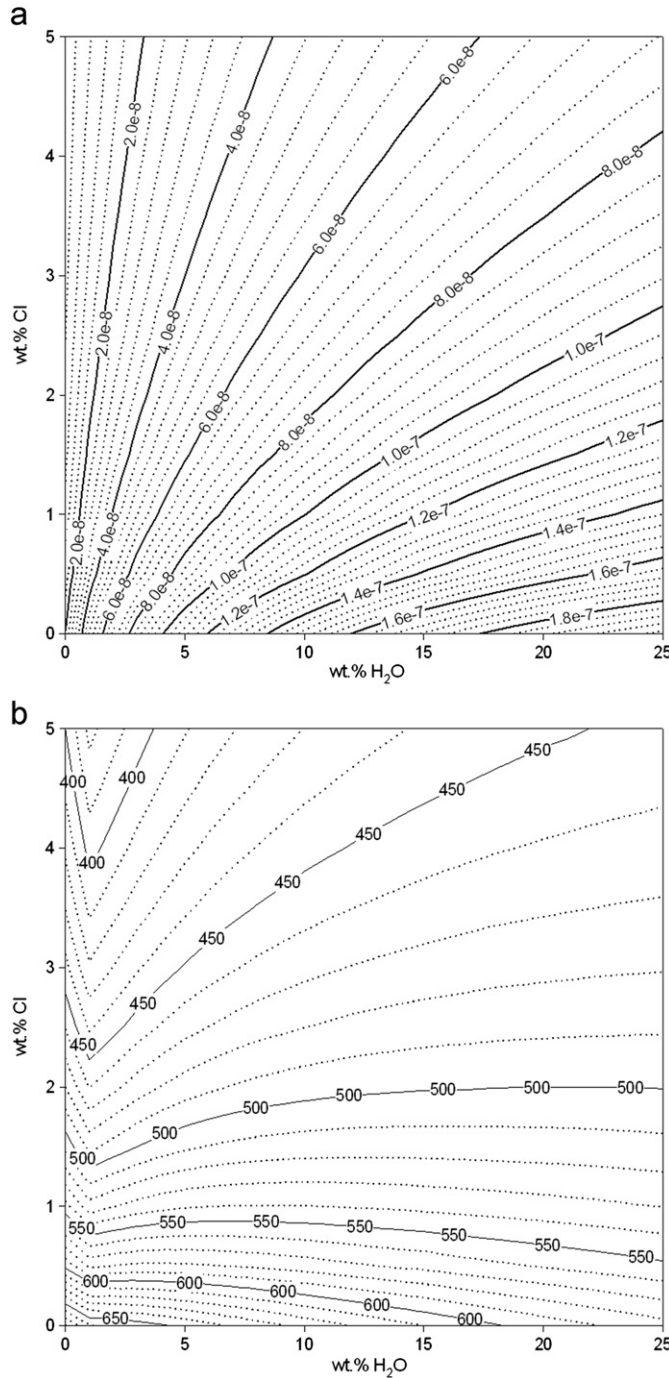


Fig. 6. (a) Contour plot showing the thermal neutron flux as a function of H₂O and Cl concentration. Values on individual contours are in units of cm²/s/source-particle and (b) contour plot showing the flux weighted time average (FWTA) as a function of H₂O and Cl. Values on individual contours are in units of microseconds. Thermal neutron die-away curves acquired by DAN will have a specific total thermal neutron flux and FWTA value. When those two contour lines are overlain on one another, the point of intersection will define the wt% H₂O and wt% Cl.

FWTA contour (intersections closer to 90° being better). By tracking changes to total neutron flux and FWTA values along traverses by the MSL rover, locations for more detailed study can be identified based on the indications of potential Cl-rich evaporites or buried hydrogen-rich materials.

The total (time-integrated) epithermal flux can also provide constraints. Epithermal neutrons are counted from DAN's cadmium-coated ³He tube (up to ~700 keV). Epithermal neutrons are primarily sensitive to the hydrogen abundance of the soil and

do not show significant variations with changes in absorption cross-section [41]. Epithermal neutron fluxes can thus be used to determine the hydrogen content, which then constrains the Cl content from the suite of paired H₂O and Cl contents allowed by the total thermal neutron flux. Determination of the FWTA for epithermal neutrons is ambiguous, as fast neutrons from the source are mixed with epithermal leakage neutrons in the first tens of microseconds after the pulse (see Fig. 2a). We have shown, however, that in die-away measurements the total epithermal neutron flux (from ~1–100 μs) is sensitive to variations in hydrogen content but does not vary significantly with Cl content (Fig. 7). Fig. 7 demonstrates the sensitivity of epithermal neutrons to H₂O content by showing both epithermal and thermal neutron fluxes for 0, 1, 2, and 3 wt% H₂O with 0 wt% Cl. Fig. 7 also shows

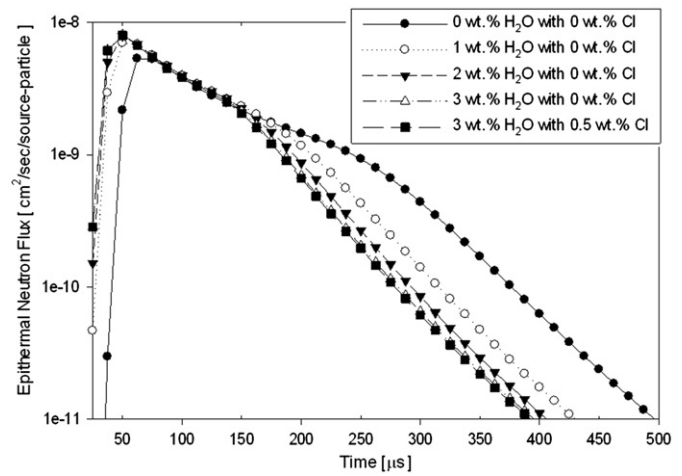


Fig. 7. Epithermal arrival times at the detector for select H₂O and Cl concentrations. Note that the addition of 0.5 wt% Cl to 3 wt% H₂O does not alter the epithermal neutron flux.

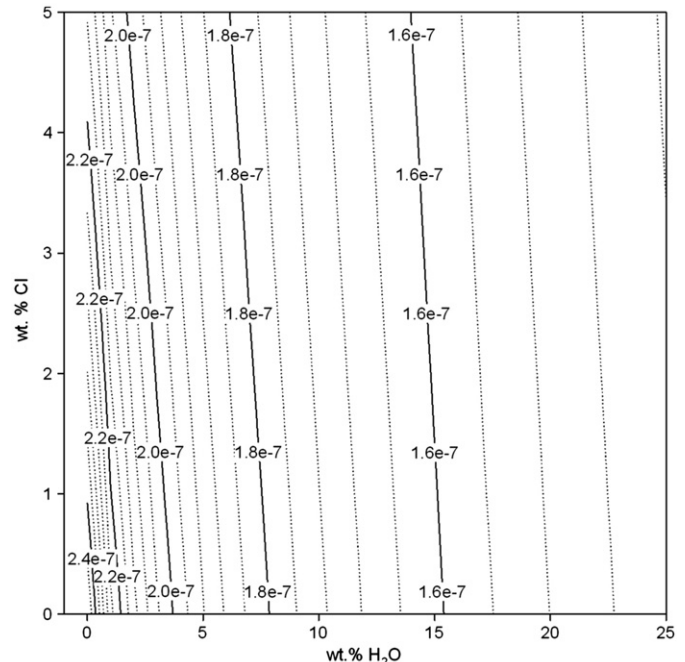


Fig. 8. Contour plot of the epithermal neutron flux as a function of H₂O and Cl showing the relative insensitivity of epithermal neutrons to Cl content. Values on individual contours are in units of cm²/s/source-particle.

the die-away curve for 3 wt% H₂O with the addition of 0.5 wt% Cl, which is indistinguishable from the neutron die-away curve for 3 wt% H₂O and 0 wt% Cl, demonstrating the insensitivity of epithermal neutrons to the presence of high thermal neutron absorption cross-section elements. Epithermal neutrons can, therefore, be used to determine whether changes in thermal neutron die-away are due to variations in hydrogen abundance or in macroscopic absorption cross-section. We have also modeled the total epithermal neutron flux for 0–25 wt% H₂O and 0–5 wt% Cl. These results are presented in Fig. 8. The epithermal neutron flux contours are nearly independent of Cl content for the range of modeled H₂O abundances, indicating that they constrain only the hydrogen content of the near surface.

4.5. Specific locations on Mars

Here we use the results from MER Spirit and Opportunity APXS geochemical data to model the thermal neutron flux for well studied, local-scale geologic features in Meridiani Planum and Gusev Crater that (1) contain unique chemistry with anomalous abundances of high neutron absorption cross section elements and (2) are thought to provide evidence for the presence or past-action of near-surface water. The geochemical compositions chosen are Eileen Dean, a subsurface Cl-rich soil identified near Home Plate within Gusev Crater; Jack Russell, a mixture of hematite-rich “blueberries” and surrounding surface materials identified within the Berry Bowl in Eagle Crater; Kenosha Comets, a buried silica-rich soil identified in a location named the Eastern Valley, within Gusev Crater; and the Heat Shield Rock Fe-rich meteorite found by the Opportunity Rover in Meridiani Planum. While there are no plans to send the MSL rover (or any other mission) to either MER landing site, these sites serve as examples of the high degree of localized geochemical variability that can be found on Mars when exploring a well-chosen site with a mobile surface mission.

4.5.1. Cl-rich Eileen dean soil

Home Plate is a region on Mars thought to harbor volcaniclastic and hydrothermally altered sediments [34]. As described in Section 4.4, Spirit has discovered several classes of rocks and soils that are relatively enriched in Cl. Cl enhancements are found in individual rocks as well as buried soils that were exposed by dragging one of the rover's wheels. We have modeled the Eileen Dean class of soils as both a thin, discrete subsurface layer (4 cm deep, 4 cm thick) and a thick subsurface layer (also buried 4 cm deep) that extends well below the depths where PNG-sourced neutrons interact. Based on the results presented in Section 4.3, the APXS-derived abundance of Cl for the Eileen Dean class of soils (1.7 wt% Cl) is high enough to have a strong effect on thermal neutron die-away. The composition of the surrounding bulk soil and the composition of Eileen Dean are shown in Table 1. Modeled thermal neutron die-away curves for the DAN neutron detectors positioned above the discrete and continuous layers of Eileen Dean composition, as well as above a homogeneous, bulk soil are presented in Fig. 9.

For the case of a continuous layer of Eileen Dean composition, the total thermal flux is reduced by ~45% relative to the homogeneous bulk soil, while for a discrete 4 cm thick layer, the total thermal flux is reduced by ~8%. For the continuous layer, the FWTA is shifted to earlier times by 13%, relative to the homogeneous bulk soil, while for the discrete layer the FWTA is shifted earlier by 2%. Comparing these changes to our results for increasing hydrogen with no Cl, a 45% decrease in total thermal flux gives the same change in FWTA as a ~5 wt% decrease in water-equivalent hydrogen in the near surface for a homogeneous

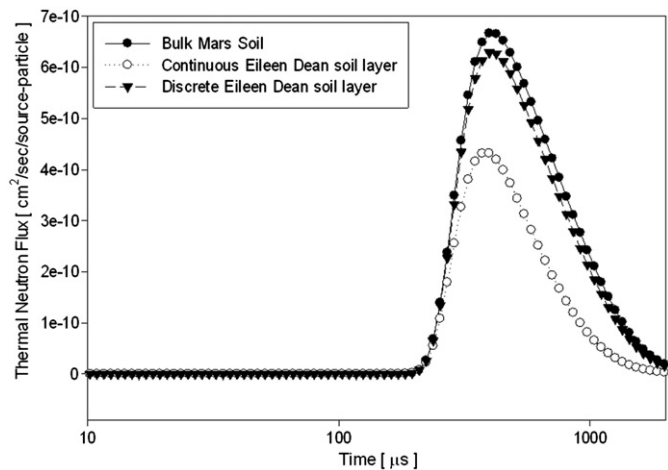


Fig. 9. Thermal neutron flux for bulk soil composition, bulk soil composition with a discrete layer (4 cm thick, 4 cm deep) of Eileen Dean composition and bulk soil composition with a continuous soil layer of Eileen Dean composition.

surface with H₂O. The FWTA, however, allows us to further interpret the cause of this decrease in thermal neutron flux. As described in Section 4.3, the FWTA decreases with increasing Cl content and increases with decreasing hydrogen content, such that the effect of the Eileen Dean layer is to shift the FWTA to earlier times. Along a traverse by MSL, if hydrogen content were to decrease DAN would observe an increase in the FWTA. Therefore, in both the continuous and discrete Eileen Dean layer scenarios, DAN would identify the presence of a high macroscopic absorption element (presumably Cl or Fe) in the near surface. There is no significant change in the epithermal neutron flux for any of these scenarios, as there is no hydrogen in any of the simulated compositions.

4.5.2. Fe-rich “blueberry”-rich soil

Pervasive surface components of Meridiani Planum are hematite concretions known as “blueberries”. These hematite-rich material spherules are observed to be eroding from outcrops, collecting on the surface as a lag deposit [24]. The unique mineralogy and chemistry of the spherules suggests that they were formed by stagnant groundwater saturating the sulfate-rich Meridiani rocks and sands, leaching Fe-oxide from these materials, and re-precipitating it in the subsurface as hematite concretions. The presence of hematite spherules at Meridiani is one of the many features discovered by the Opportunity rover that indicate interaction of water with near-surface materials. Because percolation of groundwater into the surrounding rocks is the most plausible explanation for the presence of the spherules, Fe-rich materials are likely to be present just below the surface either in outcrop or as a lag deposit that was later buried by eolian drift. Because the neutron absorption cross-section of Fe is relatively high (Table 2), we expect that if the concentration of hematite-rich materials were high, its effects would be recorded in thermal neutron die-away curves acquired by DAN. To test this hypothesis, we use a spherule-rich composition from the Jack Russell APXS observation within the Berry Bowl in Eagle Crater shown in Table 1 [24]. This observation was chosen because the surface concentration of spherules was so spatially dense that the derived chemical data can be approximated as the composition of the spherules themselves.

Fig. 10 shows the thermal neutron die-away results for three separate simulations: a bulk Mars soil, a continuous hematite-rich

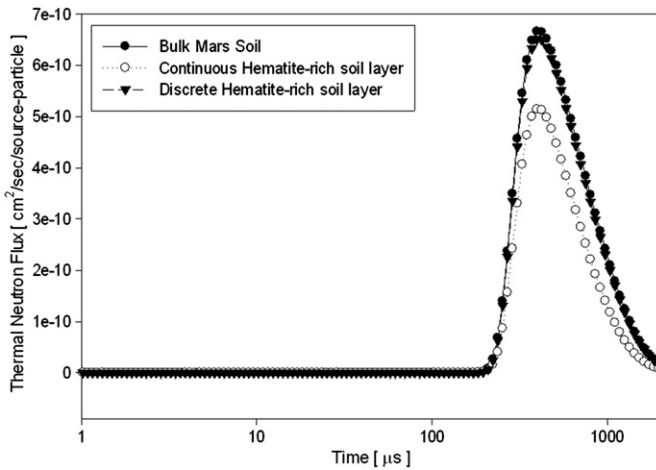


Fig. 10. Thermal neutron flux for bulk soil composition, bulk soil composition with a discrete layer (4 cm thick, 4 cm deep) of hematite-rich composition and bulk soil composition with a continuous soil layer of hematite-rich composition.

soil layer below 4 cm, and a discrete hematite-rich soil layer 4 cm deep and 4 cm thick. The effects of the hematite-rich compositions are significant, with a reduction of total thermal flux relative to the bulk soil of $\sim 30\%$ for the continuous layer and $\sim 3\%$ for the discrete layer. A shift in FWTA to $\sim 5\%$ earlier times is observed for the continuous layer, whereas there is a shift to $< 1\%$ earlier times for a discrete layer. Even with an Fe enrichment of over 10 wt% relative to the nominal Mars value, the Jack Russell composition does not influence the thermal neutron die-away curve as much as a mere 1 wt% increase in Cl from the nominal Mars Cl value, as seen in the Eileen Dean results (Section 6.3.1).

4.5.3. Si-rich, Kenosha Comets soil

The target Kenosha Comets, near Home Plate, is a light-toned soil revealed by trenching Spirit's right front wheel. APXS measurements of this remarkable material revealed it to be composed of ~ 91 wt% silica (SiO_2), indicative of an association with a past hydrothermal system [25,34]. The dominance of SiO_2 in Kenosha Comets material leaves little room for other compositions; so from a neutron perspective, Kenosha Comets is notable for its deficit of most high absorption cross-section elements (except for a small enrichment in Ti) relative to Mars bulk soil. In fact, Kenosha Comets material is also a poor moderator of neutrons relative to dry bulk Mars soil because of the near absence of Fe (which constitutes the largest scattering cross-section element in dry bulk Mars soil). We modeled neutron die-away from a layer of Kenosha Comets material buried beneath 4 cm of Mars bulk soil and found that the total thermal neutron flux was suppressed (relative to homogeneous Mars bulk soil) by over 99%, and the FWTA value was shifted earlier by 60% (Fig. 11). For a discrete layer buried at 4 cm, 4 cm thick, the thermal neutron flux is reduced by $\sim 75\%$. The FWTA is shifted to earlier times by 60% for a continuous layer relative to bulk soil and $\sim 34\%$ for a discrete layer. The huge reduction and shift in arrival times of thermal neutrons is caused by the lack of effective scattering elements available to thermalize neutrons. The presence of the high absorption cross-section element Ti acts to further reduce the population of whatever thermal neutrons are produced. The fact that Kenosha Comets material would "stand out like a sore thumb" in DAN data, even when buried just as it was found near Home Plate, it is a strong testament to DAN's ability to find geochemical anomalies that have no present H content but are critical to understanding a site's aqueous history.

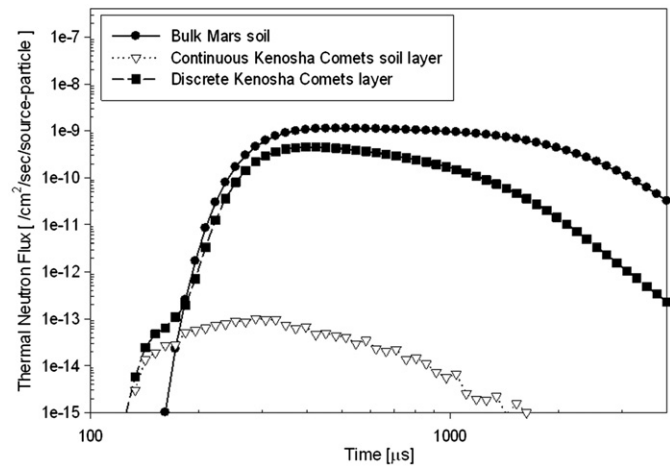


Fig. 11. Log-log plot of thermal neutron flux for bulk soil composition, bulk soil composition with discrete layer (4 cm thick, 4 cm deep) of Kenosha Comets composition and bulk soil composition with a continuous soil layer of Kenosha Comets composition.

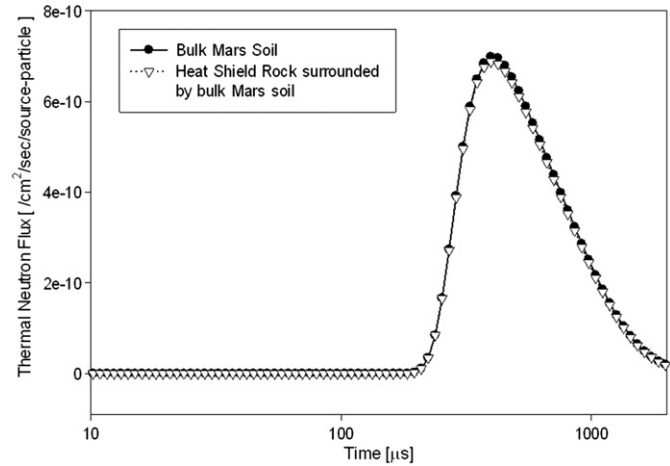


Fig. 12. Thermal flux for bulk soil composition bulk dry soil composition with shallowly buried meteorite of Heat Shield Rock composition.

4.5.4. Fe-meteorite, Heat Shield Rock

The Opportunity rover has discovered several meteorites, which were found by APXS to contain nearly 94 wt% Fe [28]. Heat Shield Rock is an iron meteorite of ~ 30 cm maximum dimension found near the lander's heat shield that was dropped during its decent to the surface. Upon initial examination the smooth, metallic surface and pitted texture suggested the rock to be a meteorite. Further mid-infrared analysis showed the rock to be of low emissivity, characteristic of metals and iron meteorites [28]. A full analysis by the APXS revealed Heat Shield Rock to have a bulk elemental composition of 94% Fe, 7% Ni, ~ 300 ppm Ge, and < 100 ppm Ga. We model Heat Shield Rock as a $30 \times 30 \times 30$ cm cube, embedded in the surface so that the top facet of the cube is flush with the surface. The cube is surrounded by bulk Mars soil. Fig. 12 shows the thermal neutron die-away results for the rover directly above the meteorite and for bulk Mars soil. The overall reduction of thermal neutron flux for the model including Heat Shield Rock material is only 0.018% relative to Mars bulk soil, while the FWTA only shifts to earlier times by 0.003%. This suggests that although Heat Shield Rock material is rich in absorbers, a $30 \times 30 \times 30$ cm³ block of it is not large enough to suppress the population of thermal neutrons created in the surrounding Mars bulk soil. As we discuss in Section 5, such small changes are not anticipated to be detectable by DAN.

5. Discussion

It is reasonable to question whether or not the effects presented in the preceding sections have the potential to be detected by DAN. Although an instrument response model is not available, several assumptions may be made based on statistics inherent to radiation detection instruments. As an estimate of the uncertainty associated with the detection of a single neutron, we assume that the counting statistics follow a Poisson distribution such that the uncertainty associated with a measurement at any given time bin is the square root of the total number of counts [8]. In addition, we assume the following operational modes for DAN: (1) a pulse rate of 10 Hz and (2) an integration time of 5 min. We also assume a modest thermal neutron detection efficiency for ${}^3\text{He}$ tubes of 95% [42]. In Fig. 10 we have shown a relatively small decrease in thermal neutron flux ($\sim 4\%$) for the presence of a discrete layer rich in hematite spherules. Assuming the above operational modes and the Poisson error, we find a count rate of 5305 counts/s and an associated uncertainty of 73 counts/s (1.4%) when the hematite layer is present. Without an Fe-rich layer, the count rate is 5768 counts/s with an associated uncertainty of 76 counts/s (1.3%). Reductions in thermal flux of $\sim 4\%$, therefore, should be detectable.

We have shown that thermal neutron counts and timing are dependent on a combination of the abundance of high absorption cross-section elements (Cl, Fe) and hydrogen. Estimates of near-surface hydrogen abundance, however, can be made using epithermal neutron die-away alone. Once constraints are placed on the hydrogen content based on epithermal neutrons, thermal neutron counts can be used to determine the macroscopic absorption cross-section of the surface. As we have shown in Section 4.2, the most likely high absorption cross-section element on Mars that will strongly influence variations in thermal neutron die-away behavior is Cl; however, observations from other rover instruments may be necessary to constrain the most plausible element. The importance of using epithermal neutrons in combination with thermal neutrons has been shown in Section 4.3, where we have demonstrated that the effects of Cl on the total thermal neutron flux are significant. A total thermal neutron flux is consistent with 5 wt% H_2O and no Cl is also consistent with 10 wt% H_2O and 0.5 wt% Cl, and a total thermal neutron flux is consistent with 10 wt% H_2O and no Cl is also consistent with almost 25 wt% H_2O and 0.5 wt% Cl.

In the absence of epithermal neutron counts, we have shown that H_2O and Cl abundances can be separately determined by the timing of thermal neutron die-away. When hydrogen abundance decreases, the FWTA shifts to later times. High absorption cross-section elements have the opposite effect, shifting the FWTA to earlier times (as well as decreasing the thermal neutron flux). Assuming that there are no changes in burial depth of H_2O or Cl, that measurements are acquired with DAN at regular intervals along a traverse, and that changes in subsurface composition are relatively gradual, then thermal neutron die-away measurements may be interpreted in the following manner: if the total thermal neutron flux increases and the FWTA shifts to earlier times, then hydrogen content is increasing. Alternatively, if the total thermal neutron flux is decreasing and the FWTA shifts to earlier times, the abundance of high absorption cross-section elements increases. There are, of course, pathologic cases where the amount of hydrogen is allowed to vary in a buried layer such that the hydrogen content is increased enough to compensate for the addition of high absorption cross-section elements. In this scenario, interpretation of DAN die-away curves will rely heavily on data from other instruments on-board MSL or assumed parameters that provide bulk geochemistries, burial depths or hydrogen content. Without fixing at least one of these parameters, there will be significant uncertainty in thermal neutron die-away

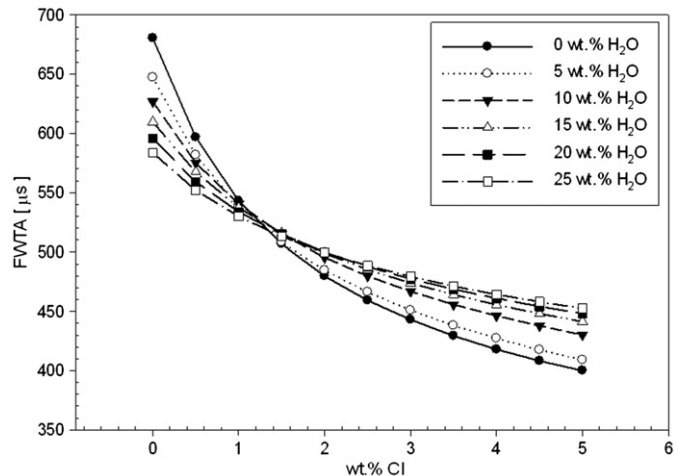


Fig. 13. FWTA versus wt% Cl for a variety of H_2O concentrations. This cross-section through the FWTA surface plot demonstrates there is an inflection around the FWTA value of 500 microseconds which can be used to constrain Cl content.

interpretations. At a minimum, our results, combined with the knowledge that both MER APXS instruments have identified up to 2.6 wt% Cl in some locations, demonstrate that the effects of elements like Cl are likely to be detectable by DAN.

The thermal neutron contour plots (Fig. 6a and b) show that the effects of hydrogen on the thermal neutron die-away curve are strongest when Cl abundances are low. The nearly vertical contours in Fig. 6a for low values of H_2O , and across all values of Cl, show that the dominant control on total thermal flux is H_2O when H_2O abundance is low. Above ~ 5 wt% H_2O , however, the effect of macroscopic absorption cross-section dominates both surface and contour plots. At values of H_2O above ~ 10 wt% the thermal flux contours in Fig. 6a are nearly horizontal, indicating that the macroscopic absorption cross-section has an increasingly dominant effect on thermal neutron flux. The FWTA contours in Fig. 6b more clearly demonstrate the abundance of Cl at which macroscopic absorption cross-section appears to have a dominant effect. At low Cl values, individual FWTA contours are nearly independent of Cl abundance (i.e., the contours are horizontal in Fig. 6b). However, at Cl abundances above ~ 1.7 wt% and H_2O abundances above ~ 1 wt%, contours are a function of both Cl and H_2O . Above this Cl abundance, the effects of macroscopic absorption cross-section dominate the range of possible FWTA values. We can use this effect to demonstrate how FWTA can constrain Cl abundance. Fig. 13 is a cross-section through the FWTA contour plot shown in Fig. 6b. For lines of constant H_2O abundance and Cl abundances from 0 to 5 wt%, FWTA values of less than ~ 500 μs all correspond to Cl abundances greater than 1.7 wt%. Conversely, FWTA values greater than ~ 500 μs correspond to Cl abundances less than 1.7 wt%. The absolute time of this diagnostic FWTA is subject to change based on the rover configuration above the ground, the accuracy of the timing electronics, the efficiency of the detectors, and the real Mars near-surface composition; however, better estimates on these conditions can be used in MCNPX simulations to solve for this diagnostic FWTA once MSL has landed, using data from the landing site as well as other MSL instruments.

6. Conclusions

We have characterized the effects of high absorption cross-section elements on thermal neutron die-away curves which are similar to those that will be acquired by the DAN instrument on-board MSL. In neutron die-away measurements, strong reductions in the total number of thermal neutrons and shifts in

the time-weighted thermal flux average are due to the presence of high absorption cross section elements (Cl, Fe) or very low amounts of neutron moderating elements. Changes in neutron flux along a traverse by MSL may be indicative of hydrothermal and evaporitic deposits, which can enrich Cl, as well as hematite concretions that result from the percolation of groundwater containing significant amounts of Fe. We have shown that the timing component of the thermal neutron die-away can be used in combination with epithermal neutron die-away curves to distinguish changes in near-surface hydrogen from changes in macroscopic absorption cross-section. These data can be used to understand the underlying causes for observed changes in thermal and epithermal neutron die-away curves acquired during the MSL mission. Our results show that DAN can not only detect changes in subsurface hydrogen content, but that epithermal and thermal neutron die-away curves can be used to identify buried Cl- or Fe-rich soils and soils that are anomalously lacking in any hydrogen or major neutron absorbing elements.

Acknowledgments

We wish to thank the NASA Graduate Student Research Grant NNX08AT42H for funding this research. We also wish to thank Jack Trombka, Ann Parsons, Richard Starr and Tim McClanahan for their help and advice throughout this work. We would also like to thank our three anonymous reviewers for their contributions and assistance improving this manuscript.

References

- [1] M.L. Litvak, et al., *Astrobiology* 8 (3) (2008) 605.
- [2] M. Golombek, et al., Overview of MSL landing sites: data products for engineering analysis, in: Proceedings of the 4th MSL Landing Site Workshop, 2010.
- [3] W.C. Feldman, et al., *Journal of Geophysical Research* 109 (E09006) (2004).
- [4] W.C. Feldman, et al., *Journal of Geophysical Research* 105 (E8) (2000) 20347.
- [5] B. Diez, et al., *Icarus* 200 (2009) 19.
- [6] I. Adler, J.I. Trombka, *Geochemical Exploration of the Moon and the Planets*, Springer-Verlag, New York, 1970.
- [7] M.W. Busch, O. Aharonson, *Nuclear Instruments and Methods in Physics Research A* 592 (2008) 393.
- [8] G. Knoll, *Radiation Detection and Measurement*, 3rd edition, John Wiley & Sons, 2000.
- [9] W.C. Feldman, et al., *Science* 297 (2002) 75.
- [10] I. Mitrofanov, et al., *Mars Odyssey*, *Science* 297 (2002) 78.
- [11] I.G. Mitrofanov, et al., *Astrobiology* 8 (#4) (2008) 793.
- [12] W.C. Feldman, et al., *Journal of Geophysical Research—Planets* 106 (E10) (2001) 23231.
- [13] D.J. Lawrence, et al., *Journal of Geophysical Research—Planets*, 111, E08001, doi:10.1029/2005JE002637.
- [14] R.C. Elphic, et al., *Geophysical Research Letters* (2007) 34. doi:10.1029/2007GL029954.
- [15] J.O. Goldsten, et al., The MESSENGER gamma-ray and neutron spectrometer, *Space Science Reviews*, 2007, doi:10.1007/s11214-007-9262-7.
- [16] David J. Lawrence, et al., Identification and measurement of neutron-absorbing elements on mercury's surface, *Icarus*, 2010, doi:10.1016/j.icarus.2010.04.005.
- [17] T.H. Prettyman, et al., *IEEE Transactions on Nuclear Science* NS-50 (#4) (2003) 1190.
- [18] W.V. Boynton, et al., *Space Science Reviews* 110 (2004) 37.
- [19] M.L. Litvak, et al., DAN/MSL instrument: road from field tests to the estimation of hydrated minerals in the Martian subsurface, in: *Proceedings of the 40th Lunar and Planetary Science Conference*, 2009, Abstract #1250.
- [20] D.J. Lawrence, et al., *Icarus* 209 (2009) 195.
- [21] B. Diez, et al., *Icarus* 196 (2) (2008) 409.
- [22] T.H. Prettyman, et al., *Journal of Geophysical Research* 109 (2004) E05001.
- [23] B.C. Clark, et al., *Journal of Geophysical Research* 87 (1982) 10059.
- [24] R. Rieder, et al., *Science* 306 (2004) 1746.
- [25] D.W. Ming, et al., *Journal of Geophysical Research* 113 (2008) E12S39.
- [26] S.W. Squyres, et al., *Science* 738 (2007) 316.
- [27] M.E. Schmidt, et al., *Earth and Planetary Science Letters* 281 (2009) 258.
- [28] C. Schroder, et al., *Journal of Geophysical Research* 113 (2008) E06S22.
- [29] H.Y. McSween, et al., *Journal of Geophysical Research* 111 (2006) E09S91.
- [30] R.V. Morris, et al., *Journal of Geophysical Research* 111 (2006) E12S15.
- [31] G.W. McKinney, et al., MCNPX Overview, LANL, Los Alamos, September 6–8, 2006, LA-UR-06-6206.
- [32] D.B. Pelowitz, et al., MCNPX User's Manual, Version 2.5.0, LANL, Los Alamos, LA-UR-05-0369, 2005.
- [33] S.W. Squyres, et al., *Journal of Geophysical Research* 111 (2006) E12S12.
- [34] S.W. Squyres, et al., *Science* 1063 (2008) 320.
- [35] H.Y. McSween, et al., *Journal of Geophysical Research* 115 (2010) E00F12.
- [36] M.M. Osterloo, et al., *Science* 319 (5870) (2008) 1651.
- [37] A. Wang, et al., *Journal of Geophysical Research—Planets* 111 (2006) E02S17.
- [38] G. Castagnoli, D. Lal, *Radiocarbon* 22 (1980) 133.
- [39] H. Vincze, et al., *Planetary and Space Sciences* 51 (2003) 375.
- [40] L.G. Evans, R.C. Reedy, J.I. Trombka, *Introduction to Planetary Remote Sensing Gamma Ray Spectroscopy*, in: C.M. Pieters, P.A.J. Englert (Eds.), *Remote Geochemical Analyses: Elemental and Mineralogical Composition*, Cambridge Univ. Press, New York, 1993, p. 167.
- [41] T.H. Prettyman et al., Mid-latitude Composition of Mars from Thermal and Epithermal Neutrons. Sixth International Conference on Mars, 2003, Abstract #3253.
- [42] W.R. Mills Jr., et al., *Review of Scientific Instruments* 33 (8) (1963).